

University of Wollongong

Research Online

Australian Institute for Innovative Materials -
Papers

Australian Institute for Innovative Materials

1-1-2018

Metal-Organic Framework-Derived Sea-Cucumber-like FeS₂@C Nanorods with Outstanding Pseudocapacitive Na-Ion Storage Properties

Zhenxiao Lu

Taiyuan University of Technology

Nana Wang

Taiyuan University of Technology, University of Wollongong, nw415@uowmail.edu.au

Yaohui Zhang

Taiyuan University of Technology

Pan Xue

Taiyuan University of Technology

Meiqing Guo

Taiyuan University of Technology

See next page for additional authors

Follow this and additional works at: <https://ro.uow.edu.au/aiimpapers>



Part of the [Engineering Commons](#), and the [Physical Sciences and Mathematics Commons](#)

Research Online is the open access institutional repository for the University of Wollongong. For further information contact the UOW Library: research-pubs@uow.edu.au

Metal-Organic Framework-Derived Sea-Cucumber-like FeS₂@C Nanorods with Outstanding Pseudocapacitive Na-Ion Storage Properties

Abstract

Sodium-ion batteries (SIBs) are supposed to be attractive energy storage and supply devices due to the abundant reserves of sodium. Their limited specific capacity and rate capacity, however, are standing in the way of the extensive application of SIBs. It is reported herein that porous sea-cucumber-like FeS₂@C nanorods can act as efficient cathode materials to satisfy the rigorous requirements of the proposed applications. The fabrication of the sea-cucumber-like FeS₂@C nanorods involves the hydrothermal growth of F-MIL (where F = Fe, MIL = materials from the Lavoisier Institute) nanorods, and subsequent sulfidation. The electrochemical results demonstrate that the FeS₂@C nanorods are an outstanding cathode material for SIBs with high specific capacity (385 mAh/g), ultralong lifetime (160 mAh/g after 10 000 cycles at 20 A/g), and exceptional rate capability. The metal-organic framework (MOF) template method provides a useful route toward the development of high-performance electrode materials with robust power and cyclability.

Disciplines

Engineering | Physical Sciences and Mathematics

Publication Details

Lu, Z., Wang, N., Zhang, Y., Xue, P., Guo, M., Tang, B., Xu, X., Wang, W., Bai, Z. & Dou, S. (2018). Metal-Organic Framework-Derived Sea-Cucumber-like FeS₂@C Nanorods with Outstanding Pseudocapacitive Na-Ion Storage Properties. *ACS Applied Energy Materials*, 1 (11), 6234-6241.

Authors

Zhenxiao Lu, Nana Wang, Yaohui Zhang, Pan Xue, Meiqing Guo, Bin Tang, Xun Xu, Wenxian Wang, Zhongchao Bai, and Shi Xue Dou

**Metal-Organic Framework-Derived Sea Cucumber-Like FeS₂@C Nanorods
with Outstanding Pseudocapacitive Na-Ion Storage Properties**

Zhenxiao Lu^a, Nana Wang^{a,b}, Yaohui Zhang^a, Pan Xue^a, Meiqing Guo^c, Bin Tang^a,
Xun Xu^b, Wenxian Wang^a, Zhongchao Bai^{a,b*}, Shixue Dou^{b*}

^aCollege of Materials Science and Engineering, Taiyuan University of Technology,
Taiyuan, 030024, PRC

^bInstitute for Superconducting and Electronic Materials, Australian Institute for
Innovative Materials, University of Wollongong Innovation Campus, North
Wollongong New South Wales 2500, Australia

^cCollege of Mechanics, Taiyuan University of Technology, Taiyuan 030024, PRC

*Corresponding author.

E-mail address: *baizhongchao@tyut.edu.cn

*Shi_dou@uow.edu.au

ABSTRACT: Sodium-ion batteries (SIBs) are supposed to be attractive energy storage and supply device due to the abundant reserves of sodium. Their limited specific capacity and rate capacity, however, are standing in way of the extensive application of SIBs. It is reported herein that porous sea cucumber-like FeS₂@C nanorods can act as efficient cathode material to satisfy the rigorous requirements of the proposed applications. The fabrication of the sea cucumber-like FeS₂@C nanorods involves the hydrothermal growth of F-MIL (where F = Fe, MIL = Materials from the Lavoisier Institute) nanorods, and subsequent sulfidation. The electrochemical results demonstrate that the FeS₂@C nanorods are an outstanding cathode material for SIBs with high specific capacity (385 mAh/g), ultralong lifetime (160 mAh/g after 10000 cycles at 20 A/g) and exceptional rate capability. The metal-organic framework (MOF) template method provides a useful route towards the development of high performance electrode materials with robust power and cyclability.

KEYWORDS: Sodium ion battery, MOFs, FeS₂@C nanorods, ultralong lifetime, Pseudocapacitance.

■ INTRODUCTION

Extensive utilization of environmentally-friendly renewable energy including wind, wave, solar power, etc. demands efficient and large-scale energy storage devices because of the intermittency and instability of these forms of energy. Rechargeable batteries with long cycling stability and high energy density are considered ideal bridges to integrate renewable energy into grids.¹⁻⁶ The high price caused by extensive consumption and the limited geographic distribution of lithium, however, makes

current lithium ion batteries (LIBs) not suitable for large-scale energy storage.⁷ Sodium, as an alkali metal like lithium, possesses similar physicochemical properties to lithium and is more cost-effective.⁸ Thus, SIBs are regarded as a promising substitute for LIBs in large-scale energy storage applications.⁹ Suitable electrode materials are the key to achieving ideal SIBs battery performances in such aspects as high power and long cycling life.⁸ On the cathode side, however, the specific capacity is limited (often lower than 200 mAh/g), because of the intrinsic drawback of intercalation-type cathodes, which can only take up one sodium ion per transition metal core.⁹ Therefore, conversion-reaction type materials are more attractive because they can accommodate more than one Na^+ per transition metal core, resulting in higher theoretical capacities. Among all the conversion-reaction type materials, FeS_2 is the most attractive because it is very cheap, naturally abundant, and environmentally benign. However, most of the reported FeS_2 has showed poor electrochemical performance with large irreversibility and fast capacity decay during cycling because of large volume changes and low electrical conductivity. Therefore, developing optimized structures to facilitate ion/electron transmission and tolerate repeated Na^+ insertion/extraction is a precondition for realizing the above-mentioned superiority of iron chalcogenides electrode.

Generally speaking, two main strategies are applied to improve the electrochemical performance of FeS_2 . One is to design nanostructure to shorten ion/electron transport paths. Another is to form smart combination of FeS_2 with other electrically conductive materials to increase the electrical conductivity^{10, 11}. Pint's group reported

that decreasing the size of FeS_2 can boost the reversibility of the conversion reaction process. Their ultrafine FeS_2 (2–9 nm) exhibited improved electrochemical performances due to the short diffusion length.¹² Zhu et al. synthesized FeS_2 wrapped in a carbon coating to enhance the electrical conductivity and solve the problem of soluble polysulfide dissolution, thus improving the electrochemical performance.¹³ Recently, using ether-based electrolyte greatly improved the performance of FeS_2 based materials.¹⁴ Although great success was achieved, FeS_2 electrode still far from practical application. Therefore, to develop a new type of FeS_2 electrode with good cycling stability and high rate capability for SIBs is urgent.

Here, porous sea cucumber-like $\text{FeS}_2@\text{C}$ nanorods constructed by growing $\text{FeS}_2@\text{C}$ nanoflakes on $\text{FeS}_2@\text{C}$ nanorods were synthesized through a hydrothermal process for preparing uniform F-MIL nanorods and a subsequent sulfidation process. The featured nanostructure has many advantages as electrode for batteries. Firstly, the porous structure can efficiently shorten the ion insertion distance, provide more active sites and buffer the volume change during the electrochemical reaction.¹⁵⁻²³ Secondly, the well-connected carbon networks can not only facilitate charge transport and mass transfer, but also help to stabilize the formed solid electrolyte interphase (SEI) layer.²⁴⁻²⁷ Thirdly, the $\text{FeS}_2@\text{C}$ nanoflakes enlarge the contact area between the electrolyte and the electrode, thus improving the electrochemical performance of the composite. Consequently, the porous sea cucumber-like $\text{FeS}_2@\text{C}$ nanorods delivered outstanding sodium storage properties, including high specific capacity (385 mAh/g), long cycling stability (160 mAh/g after 10000 cycles at 20 A/g), and superior rate

capability. Our work offers a paradigm of a smart SIBs cathode material that greatly promotes the battery performance.

■ MATERIALS AND METHODS

Materials and Preparation of FeS₂@C Nanorods. The F-MIL nanorods were prepared by a simple hydrothermal method. 0.5406 g FeCl₃·6H₂O and 0.4153 g 1,4 benzene dicarboxylic acid (1,4 H₂bdc acid) were dissolved in 27 mL dimethyl formamide (DMF) through ultrasonic dispersion and stirring. Then, 3 mL of 0.4 mol/L NaOH solution was dropped into the above mixture. After stirring for several minutes, the final solution was transferred into a Teflon-lined autoclave and heated at 100 °C for 12 h in an oven. The pink product was collected after washing with DMF for three times to remove impurities and dried at 60 °C overnight, to finally yield the F-MIL nanorods. Appropriate amounts of F-MIL and sulfur powder were placed in a combustion boat and annealed at 500 °C for 2 h in nitrogen with a heating rate of 2 °C/ min. The black product was collected and washed with formaldehyde to remove the residual sulfur and leave the sea cucumber-like FeS₂@C nanorods.

Morphology and Structure Characterization. The components of the product were identified by X-ray diffraction (XRD; Bruker D8 ADVANCE) with Cu K α radiation (λ = 0.15418 nm), Raman spectroscopy (NEXUS 670 Micro-Raman Spectrometer), thermogravimetric analysis (TGA; Mettler Toledo TGA/SDTA851 thermal analyzer apparatus) conducted in air and X-ray photoelectron spectroscopy (XPS; Thermo Scientific K-Alpha spectrometer using Al K α as the X-ray source). A JEOL-1011 transmission electron microscope (TEM) and a JSM-7600F JEOL

scanning electron microscope (SEM) were used to characterize the morphology of the precursor and the final product after sulfidation. High resolution TEM (HRTEM) measurements were conducted on a JEOL-2110 high-resolution transmission electron microscope with an acceleration voltage of 200 kV to gain insight into the subtler aspects of the structure and the crystallinity.

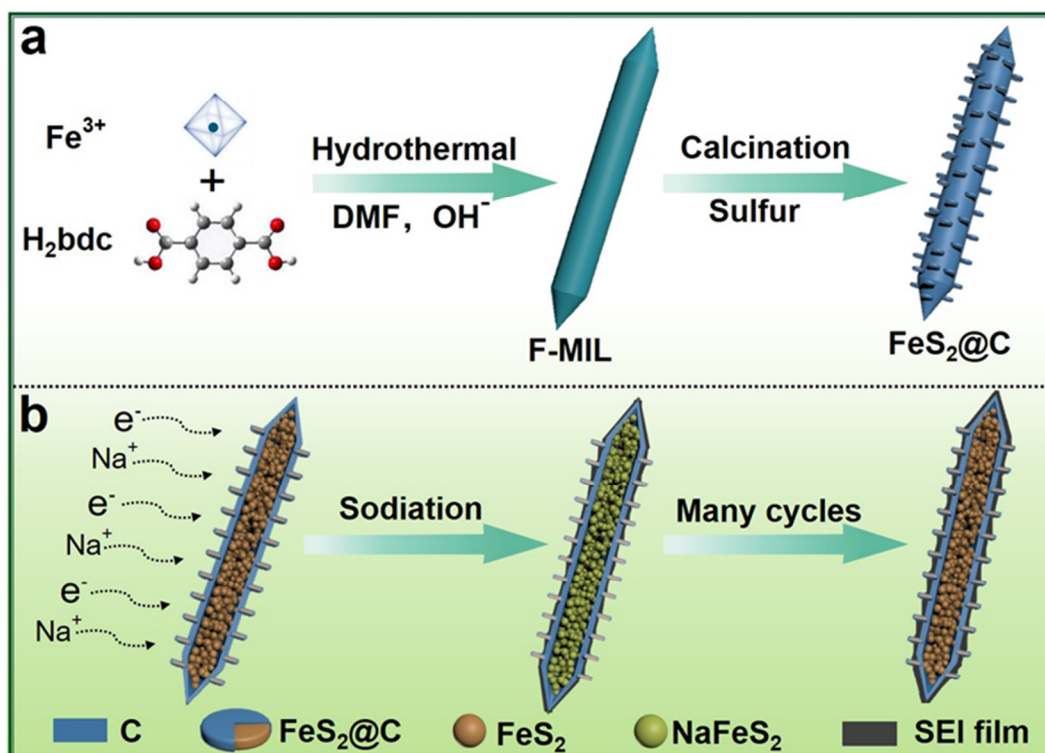
Preparation of Electrodes. The electrodes were fabricated by mixing FeS₂@C nanorods, carbon black, and carboxymethyl cellulose (CMC) in weight ratio of 7:2:1 with deionized water as solvent, and the resultant slurry was coated on a copper foil before drying in a vacuum oven at 60 °C for 6 h. The electrochemical measurements were conducted on CR2032 coin-type cells, which contained the as fabricated electrode (with active material mass loading of ~1 mg/cm²), pure Na foil as counter electrode, Whatman GF/F as separator, and 1M NaCF₃SO₃ in diethylene glycol/dimethyl ether (DEG/DME) as electrolyte. Charge-discharge tests were conducted on a LAND multi-channel battery measurement system at different constant current densities within a voltage window of 0.8-3 V at 25 °C. The Cyclic voltammograms (CVs) of the batteries were collected on a CHI-760 electrochemical workstation at scan rates ranging from 0.1 mV/s to 10 mV/s.

■ RESULTS AND DISCUSSION

Phase and Morphology Characterization. The detailed synthesis process for FeS₂@C nanorods is schematically illustrated in Scheme1. Firstly, the iron is incorporated in organic molecules during the hydrothermal process to form F-MIL nanorods, which delivers a stable porous structure and high surface area.²⁸⁻³¹

Afterwards, the needle-shaped F-MIL nanorods were calcined under nitrogen atmosphere in the presence of sulfur to obtain the sea cucumber-like FeS₂@C nanorods. During the calcination, the organic complex (bdc) in F-MIL was carbonized to form a carbon shell at 500 °C, while the Fe³⁺ was reduced and combined with S via the Fe-S bonds to form FeS₂ nanoparticles dispersed in the carbon shell. Additionally, FeS₂@C nanoflakes formed on the surface of the FeS₂@C nanorods. As revealed in Scheme 1(b), the-obtained FeS₂@C nanorods featured with loose FeS₂ nanoparticles encapsulated in carbon shells and FeS₂@C nanoflakes dispersed on the surfaces of the nanorods, resulting in the sea cucumber-like structure. Such a special structure imparts several advantages when used as electrode for batteries: firstly, the nano-sized FeS₂ particles inside the carbon shell efficiently accelerate the transportation of Na⁺ and electron; secondly, the interspace between the FeS₂ particles could buffer the volume expansion caused by sodiation and facilitate electrolyte permeation;³² thirdly, the carbon shell improves the electrical conductivity of the electrode and is beneficial for growth of the SEI film on the outer surface, guaranteeing sufficient internal space for FeS₂ particle expansion.^{27, 33-35} Therefore, the FeS₂@C nanorods deliver a comparable specific capacity, superior rate capacity and outstanding cycling stability as electrode for SIBs.

Scheme 1. Schematic illustration of the (a) synthesis procedure and (b) advantages when used as electrode for FeS₂@C nanorods.



In order to reveal the components and crystallographic structure of the product after sulfidation, XRD testing was conducted as exhibited in Fig. 1a. The distinct strong peaks demonstrate the high crystallinity of the as-prepared FeS₂@C nanorods, which can be indexed to FeS₂ (JCPDF No. 65-3321) and FeS₂ (JCPDF No. 65-2567). Peaks for the carbon layer are not detected in the XRD pattern because of the amorphous structure of the carbon. However, the peaks located at 1314 and 1544 cm⁻¹ in the Raman spectrum (Fig. 1b) are characteristic of carbon and indicate the presence of the carbon layer.³⁶ The small peaks at 336 and 382 cm⁻¹ are derived from FeS₂.³⁷ The content of FeS₂ in the FeS₂@C nanorods can be determined by means of thermogravimetric analysis (TGA) (Fig. S1 in the Supporting Information). According to the XRD pattern of the annealed FeS₂@C nanorods (Fig. S2 and S3), the weight loss from 200 °C ~ 450 °C is attributable to the comprehensive effect of the transformation of FeS₂ to Fe₂(SO₄)₃ and the partial oxidation of C. The subsequent

weight loss at 550 °C ~ 600 °C was due to the thorough decomposition of $\text{Fe}_2(\text{SO}_4)_3$ into Fe_2O_3 and the oxidation of C to carbon oxides. Thus, the content of FeS_2 in the as formed $\text{FeS}_2@\text{C}$ nanorods is 79.9 % based on the law of conservation of mass.³⁸ The specific surface area and pore-size distribution of the porous $\text{FeS}_2@\text{C}$ nanorods were revealed by BET method. The type \square N_2 sorption isotherms displayed in Fig. S4 indicate that the $\text{FeS}_2@\text{C}$ nanorods possess a specific surface area of 103.7 m^2/g . And the inserted pore-size distribution curve, which based on the BJH method, confirmed that the pore diameter of the $\text{FeS}_2@\text{C}$ is ≈ 12 nm.

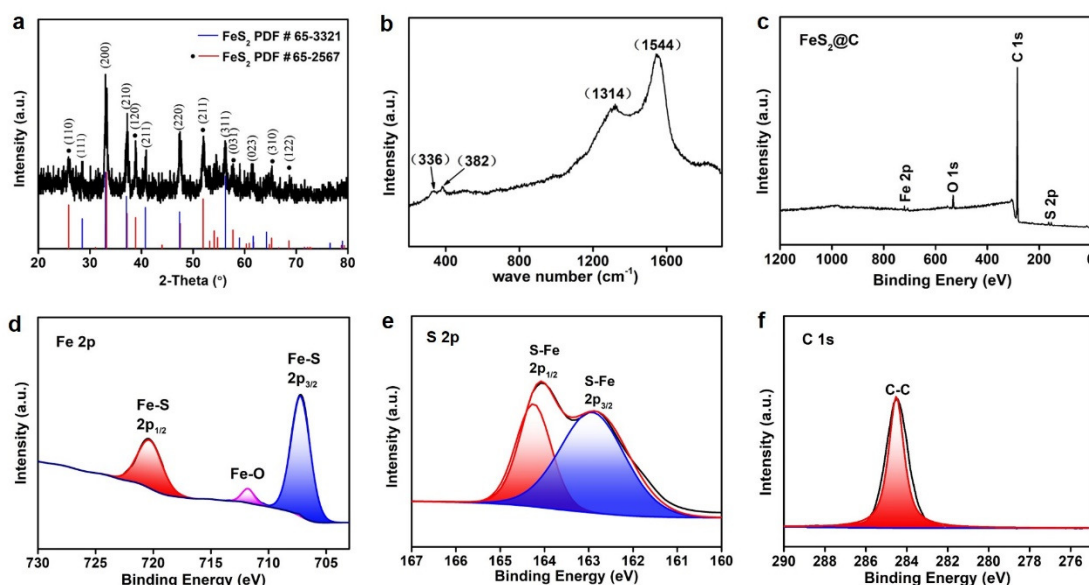


Fig. 1. (a) XRD pattern and (b) Raman spectrum of the of $\text{FeS}_2@\text{C}$ nanorods. XPS spectra of the $\text{FeS}_2@\text{C}$ nanorods: (c) survey (d)Fe 2p, (e) S 2p, and (f) C 1s.

The components and chemical state of the sample were further characterized via XPS analysis. Fig. 1c shows the survey XPS spectrum of the $\text{FeS}_2@\text{C}$ nanorods, which matches well with the XRD pattern except for slight oxygen pollution due to oxidation of $\text{FeS}_2@\text{C}$ in the air. The two peaks of Fe 2p (Fig. 1d) located at 720.63 eV and 707.33 eV correspond to $\text{Fe } 2p_{1/2}$ and $\text{Fe } 2p_{3/2}$ orbitals, indicating the existence of Fe^{2+} . And a small peak located at 711.19 eV was observed, which is due to the Fe-O

contation at the surface of FeS₂@C and the oxygen-containing functional groups.^{39,40} The XPS specturn of S 2p (Fig. 1e) exhibits two peaks located at 163.83 eV and 162.45 eV, representing S 2p_{1/2} and S 2p_{3/2}, respectively, which is in agreement with the sulfur binding energy of FeS₂.³⁹ Fig. 1f shows the XPS spectrum of carbon, in which the peak (284.6 eV) is consistent with the binding energy of carbon. These results further confirm the composition of FeS₂@C nanorods.

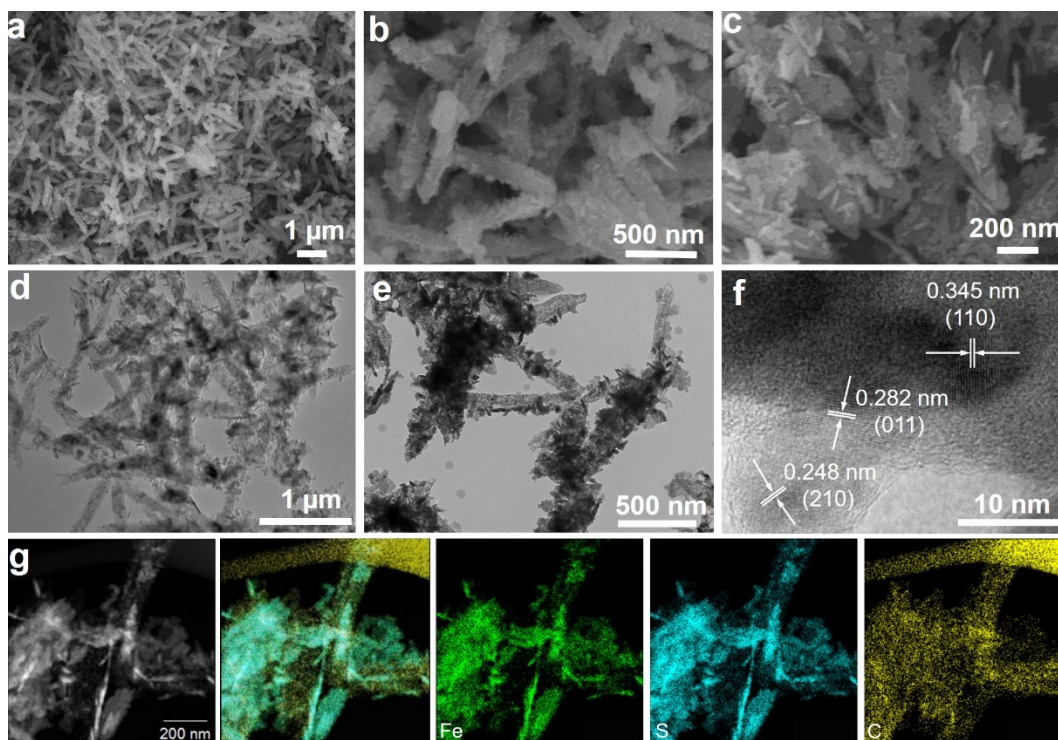


Fig. 2. (a, b and c) SEM images, (d, e and f) HRTEM images and (g) element mapping of FeS₂@C nanorods.

The morphology features of F-MIL nanorods and FeS₂@C were characterized by SEM and TEM at different magnifications. The precursor shows a uniform needle-like one-dimensional structure with length of about 1 μm and diameter of 100 nm (Fig. S5). After the sulfurization, the sample basically maintains the original one-dimensional structure and the particle size (length of 1 μm and diameter of 100 nm) (Fig. 2a and b), although the surface of sample becomes very coarse (Fig. 2b). Close observation reveals that some nanoflakes have grown on the surface of the

sample, forming a sea cucumber-like structure. The microstructure of the final product was further investigated via TEM and HRTEM. Interestingly, it should be noted that the solid F-MIL nanorods are converted into porous nanorods encapsulating scattered FeS₂ particles (Fig. 2d and e) with space between them (Fig. S6a-c). In addition, abundant plenty of nanoflakes dispersed over the surface of the nanorods, which were demonstrated to be FeS₂ covered by a thin carbon layer (~1.31 nm) by HRTEM images and element mapping (Fig. S6d, Fig. S7). The formation of the porous structure is due to the Kirkendall effect as previously reported.¹⁵ Such a porous structure could facilitate permeation of the electrolyte into the inner spaces of the nanorod and contribute to sufficient contact surface between the electrolyte and the electrode material.¹⁷ Fig. 2f is a HRTEM image of the crystalline core with clear lattice fringes and amorphous edges, which reflect the carbon shell outside the FeS₂@C nanorods. The interplanar spacings of 0.345 nm and 0.282 nm were indexed to (110) and (011) planes of FeS₂ (JCPDS No. 65-2567), respectively. The 0.248 nm interplanar spacing can be assigned to (210) planes of FeS₂ (JCPDS No. 65-3321). The element mapping displayed in Fig. 2g reveals that Fe and S are distributed under the C coating layer, which is consistent with the HRTEM images.

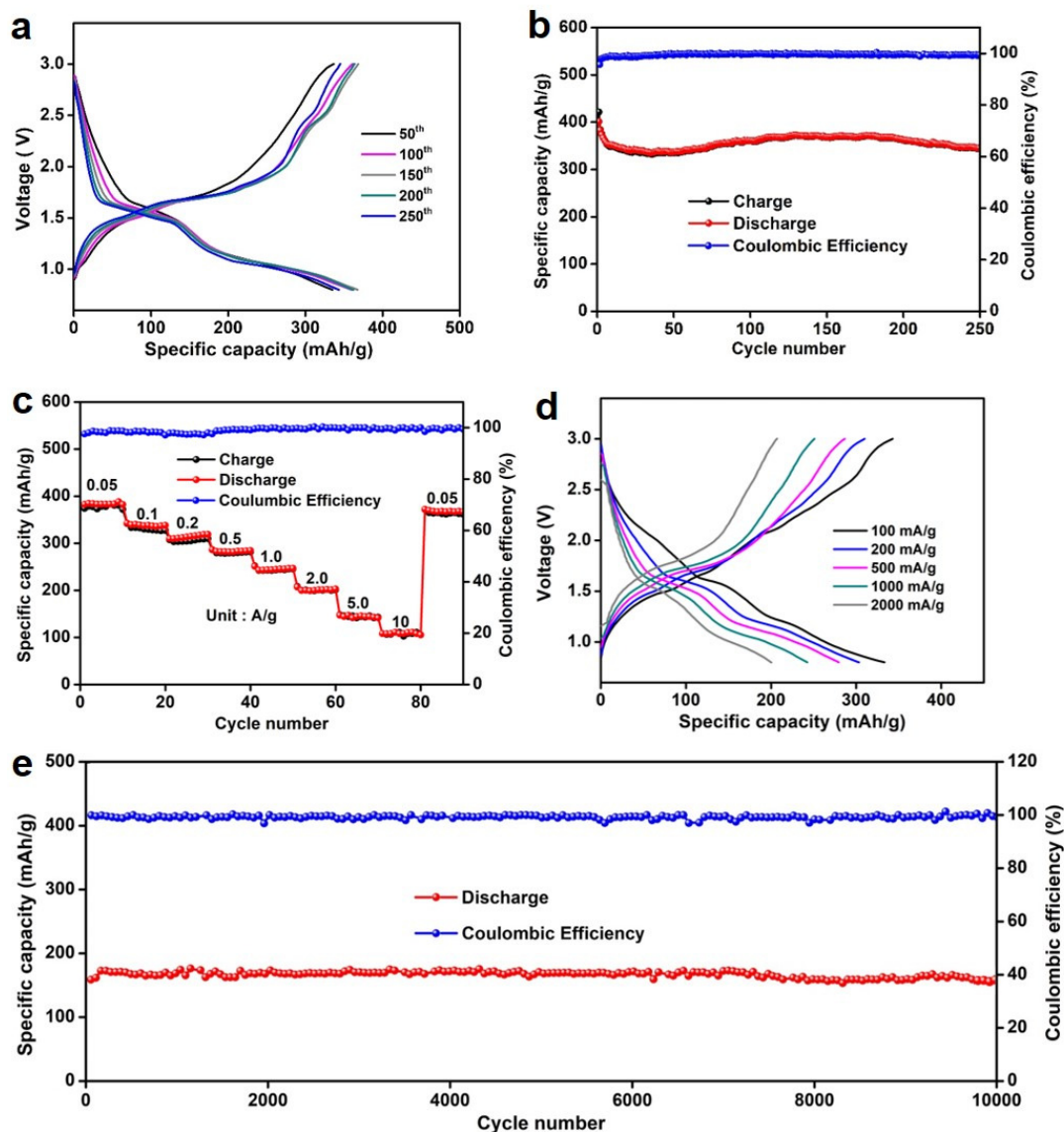


Fig. 3. (a) Charge and discharge curves of FeS₂@C/Na battery at 0.5 A/g. (b) Specific capacity and charge/discharge efficiency of FeS₂@C/Na battery at 0.5 A/g. (c) Rate capacity at current densities varying from 0.05 to 10 A/g. (d) Voltage profiles at different rates. (e) Long cycling performance at the high rate of 20 A/g.

Electrochemical Properties. The electrochemical properties of the sea cucumber-like FeS₂@C nanorods in SIBs were examined via fabricating FeS₂@C/Na batteries. Galvanostatic cycling profiles of the 1st, 2nd, 3rd, 4th, 50th, 100th, 150th, 200th and 250th cycles for the FeS₂@C electrode with a voltage window between 0.8-3 V at

current density of 0.5 A/g are displayed in Fig. 3a and Fig. S8a. The initial discharge profile displays a steep slope from 2.0 V to 1.2 V followed by a long platform which may due to the reaction of embedded Na^+ with FeS_2 ($\text{FeS}_2 + \text{Na}^+ + \text{e}^- \rightarrow \text{NaFeS}_2$) and a discharge capacity of 422 mAh/g is finally achieved.^{41, 42} As for the subsequent charge profile, a distinct platform at 2.6 V and two small plateaus at 1.6 V and 2.2 V can be detected, which correspond to the multistep Na^+ deintercalation from NaFeS_2 and formation of the Na_xFeS_2 ($x \approx 0.2$).⁴¹ These plateaus restore 95% of the discharge capacity and a gain in capacity of 402 mAh/g. In the subsequent three cycles, the discharge profiles are similar (with a plateau at 2.1 V) but they are completely different from the first discharge profile, manifesting that some irreversible change occur in the electrode after the first discharge.⁴³ However, the charge/discharge profiles after 50 cycles tend to be stable and are quite different from the first few cycles, demonstrating a gradual electrode activation process, which has been reported before.³³ Accordingly, the electrochemical reaction accompanying the Na^+ intercalation and deintercalation that occur in the FeS_2/Na batteries become stable after about 50 cycles. The plateaus at 1.5 V and 0.9 V on the 50th discharge profile represent the Na^+ stepwise intercalation and the formation of Na_xFeS_2 ($x \approx 1.6$), while the two plateaus at 1.5 V and 1.7 V on the charge profile represent the Na^+ deintercalation and the formation of Na_xFeS_2 ($x \approx 0.2$).⁴⁰ This result is also agreement with our CV test, which will be discussed later. The cyclability of $\text{FeS}_2@\text{C}$ electrode at current density of 500 mA/g is shown in Fig. 3b. The capacity degenerate in the first 30 cycles, but there is a following gradual rise, which may correspond to the slow

activation and phase change of the electrode.^{33, 41} Besides, the additional formation of SEI layer after the initial several cycles may also cause capacity increase.

The rate capability of the assembled FeS₂@C/Na batteries was investigated and is shown in Fig. 3c. In every stage of current density, the sample displays very stable cyclability with Coulombic efficiencies above 98%. Average reversible capacities of 384, 340, 310, 287, 243, 200, 147 and 108 mAh/g were achieved, at current densities of 0.05, 0.1, 0.2, 0.5, 1.0, 2.0, 5.0, and 10 A/g, respectively (Fig. 3c). Additionally, when the current was changed from 10 A/g to 0.05 A/g after 80 charge-discharge cycles, the capacity was almost fully restored, demonstrating that the electrode can tolerate a wide range of current densities. As the current density increased from 0.1 A/g to 2 A/g, the charge-discharge voltage profiles still had similar shapes, but with increasing of the voltage offset (Fig. 3d). This was mainly due to deteriorations through polarization and mechanical energy dissipation aroused by the charge-discharge cycles, which resulted in a stress effect.⁴⁴ The voltage offset decreases the energy efficiency of the cell and can be reduced by further improving the kinetics of the electrode.¹³

It is important but challenging to realize long cycling capability at high rates for current SIBs, owing to the unhelpful side reactions that occur during long cycle life. The FeS₂@C/Na batteries maintained a high capacity of 160 mAh/g after an ultralong lifespan of 10000 cycles at current density of 20 A/g (Fig. 3e) and 265 mAh/g after 2700 cycles at current density of 5 A/g (Fig. S9). The Coulombic efficiency was higher than 99% during the cycling. To the best of our knowledge, such cycling

performances are better than those of most reported SIBs (Fig. S10). This outstanding high rate cycling property probably benefits from the unique structure of FeS₂@C. Firstly, the carbon layer can not only enhance the electrical conductivity, but also accommodate the volume variation of FeS₂ during the cycling. Secondly, the small FeS₂ particles inside the carbon shell provide shortened Na⁺ and electron transport pathways, which can boost the sodium insertion/extraction. Thirdly, the open structure of the nanoflakes on the surface can enlarge the contact area between the electrode and electrolyte. Most importantly, the unique structure remains almost unchanged after charge-discharge cycling (Fig. S11).

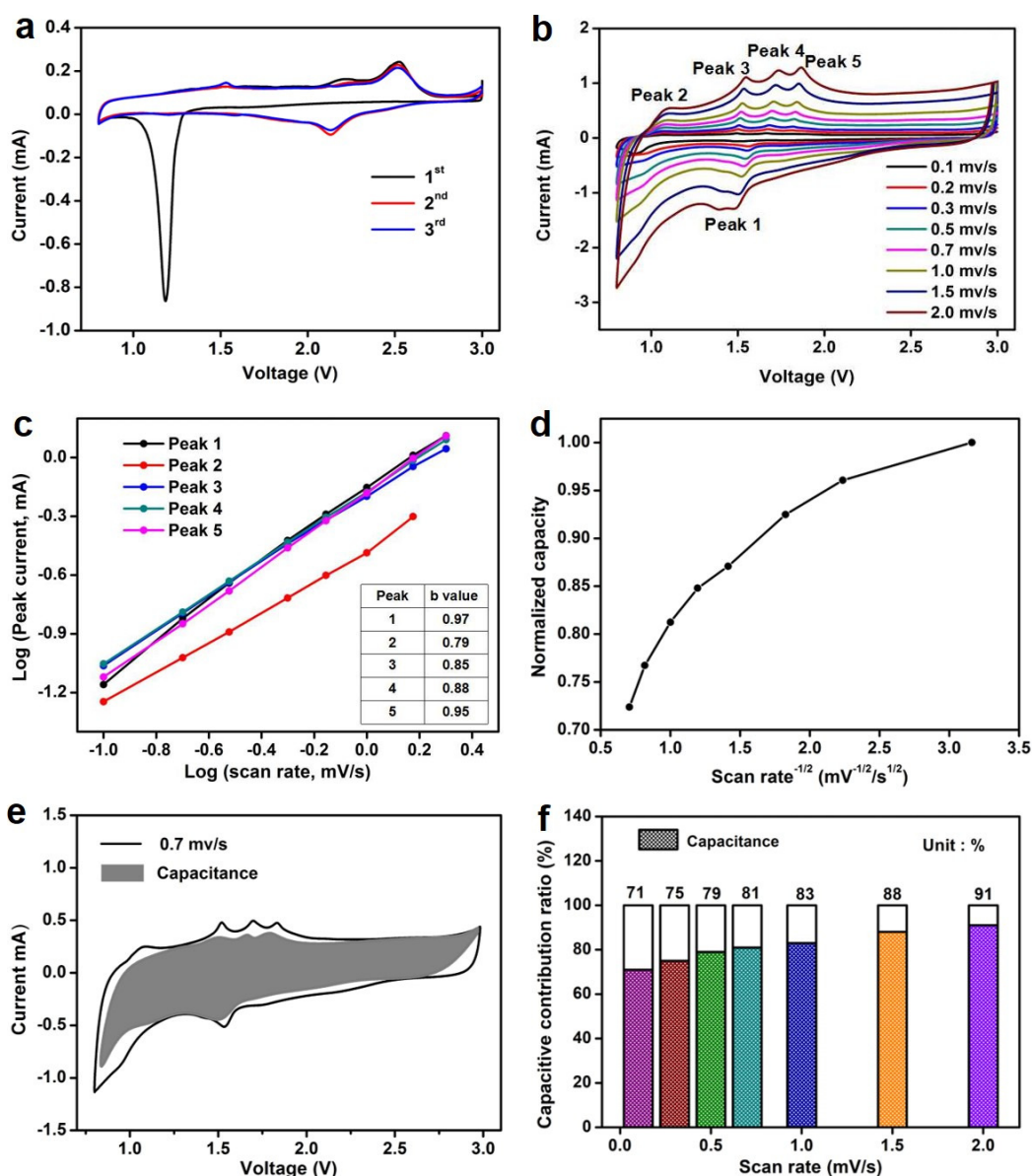


Fig. 4. (a) CVs of the $\text{FeS}_2\text{@C}$ electrode in SIB at scan rate of 0.1 mV/s and potential range of (0.8-3 V). (b) CVs after 200 cycles of the $\text{FeS}_2\text{@C/Na}$ cells at various scan rates ranging from 0.1 to 2.0 mV/s. (c) b values of each current peak. (d) Normalized capacity versus $(\text{scan rate})^{1/2}$. (e) Capacitance controlled current in $\text{FeS}_2\text{@C}$ at scan rate of 0.7 mV/s. (f) Capacitive contribution ratio at different scan rates.

Kinetic Analysis. To gain insight into the fabulously quick and vast Na^+ storage properties of the $\text{FeS}_2\text{@C}$ nanorods, the Na^+ kinetic were analyzed by CV

investigations.^{45, 46} Fig. 4a displays the initial three CVs of the FeS₂@C/Na batteries with voltage window of 0.8 to 3 V. The first discharge profile delivers a reduction peak at 1.2 V, corresponding to the phase transition of FeS₂, and the subsequent charge profile contains three oxidation peaks located at 1.6, 2.2, and 2.6 V, attributed to multistep Na⁺ deintercalation from the host material. The reduction peak at 1.2 V moves to 2.2 V in the following discharge profile due to the gradual phase transformation, while the oxidation peaks maintain their previous position and shape because the conversions are repeatable.^{12, 47} Fig.4b shows CV curves of FeS₂@C/Na after 200 cycles at different scan rate ranging from 0.1-2.0 mV/s, with four oxidation peaks located at 1.1 V, 1.51 V, 1.69 V and 1.83 V (peak 2, peak 3, peak 4 and peak 5), and one reduction peak centered at 1.54 V (peak1). This is very different from the curves of the initial cycles because of the gradual phase transformation, which is consistent with the charge/discharge profiles shown in Fig. 3a and Fig. S7a.

CV curves of FeS₂@C/Na after 200 cycles at various scan rates from 0.1 to 10 mV/s share a very similar rectangle shape with four oxidation peaks and one reduction peaks (Fig.4b and Fig. S12). It is fascinating to note that the all the small peaks are nearly identical when the scan rate increases from 0.1 to 10 mV/s (inset of Fig. 4b and Fig. S10), indicating low polarization at high rates. The relationship between the current i corresponding to a fixed voltage and scan rate ν can be characterized as:

$$i = a\nu^b \quad (1)$$

in which a and b are adjustable parameters. The b value determines whether

capacitance behavior exist at a certain voltage: $b=0.5$ means that Na^+ diffusion control the electrochemical reaction, while $b=1$ means that capacitance is dominant.^{41, 48} The calculated b values of the five peaks are between 0.79 and 0.97 (Fig.4c), revealing that the capacity originates partly from the capacitance contribution rather than arising completely from diffusion contribution.^{49, 50} This pseudocapacitive feature is in agreement with the fact that capacity does not fade significantly as the scan rate ranges from 0.1 mV/s to 2 mV/s (Fig. 4d).

The current i at a certain voltage consists of two parts: k_1v (the capacitance dominated part) and $k_2v^{1/2}$ (the diffusion-controlled part).

$$i = k_1v + k_2v^{1/2} \quad (2)$$

On the basis of this equation, the relative contributions from surface control (the capacitive part) and diffusion control (Na intercalation) at a certain potential can be determined.^{50, 51} As displayed in Fig. 4e, the capacitance contribution to the total capacity at the scan rate of 0.7 mV/s indicates that the current is capacitance dominated (k_1v). Similarly, the capacitance contribution to the capacity at various scan rate can be quantified and is exhibited in Fig. 4f. The quantified results (Fig. 4f) show that the capacitive contribution increases gradually as the scan rate is speeded up, finally achieving a maximum value of 92% at 2 mV/s.

■ CONCLUSION

In conclusion, porous $\text{FeS}_2@\text{C}$ nanorods with $\text{FeS}_2@\text{C}$ nanoflakes spreading on the outside surface were synthesized through a simple hydrothermal and annealing process. The as-synthesized $\text{FeS}_2@\text{C}$ nanorods delivered an exceptional rate capacity

of 265 mAh/g and 160 mAh/g in SIBs at 5 A/g and 20 A/g, respectively. Significantly, the FeS₂@C/Na batteries demonstrated spectacular longevity: 2700 cycles at 5 A/g and 10000 cycles at 20 A/g. Kinetic analysis explains the fantastic cycling performance of the FeS₂@C electrode through investigating the faradaic pseudocapacitance behavior in FeS₂@C/Na batteries and the great contribution of capacitive charge to capacity. The pseudocapacitance behavior is highly conducive to large current charging and long-term supply of energy. Our work provides a new choice for SIB cathode materials and goes a step further towards realizing fast charging and long-term working energy supplies.

■ ASSOCIATED CONTENT

Supporting Information

Supporting Information Available: TGA, BET results, TEM, HRTEM images and element mapping of FeS₂@C nanorods, XRD pattern of calcined FeS₂@C nanorods, SEM images of F-MIL, additional Charge/discharge curves, CV curves and cycle performance of the FeS₂@C/Na battery, SEM images of cycled electrode material, and detailed comparison with relative works

■ AUTHOR INFORMATION

Corresponding authors

E-mail: *baizhongchao@tyut.edu.cn (Bai Z. C.)

E-mail: *Shi_dou@uow.edu.au (Dou S. X.)

ORCID

Bai Zhongchao: 0000-0001-6023-9900

Notes

The authors declare no competing financial interest.

■ ACKNOWLEDGMENTS

This work was supported by National Nature Science Foundations of China (No. 51671140 and 51301117), International Cooperation Project Foundation of Shanxi Province China (No. 201603D421037), Higher School Science and Technology Innovation Project Foundation of Shanxi Province, China (No. 2016128), Research Project Supported by Shanxi Scholarship Council of China (No. 2015-034), Australian Research Council(ARC) through Discovery Projects (DP160102627), and Linkage Projects(LP160100273).

■ REFERENCE

- (1) Kim, H.-S.; Cook, J. B.; Lin, H.; Ko, Jesse S.; Tolbert, Sarah H.; Ozolins, V.; Dunn, B. Oxygen Vacancies Enhance Pseudocapacitive Charge Storage Properties of MoO_{3-x} . *Nat. Mater.* **2016**, *16*, 454-460.
- (2) Bruce, P. G.; Scrosati, B.; Tarascon, J. M. Nanomaterials for Rechargeable Lithium Batteries. *Angew. Chem. Int. Ed.* **2008**, *47*, 2930-2946.
- (3) Dunn, B.; Tarascon, J. M. Electrical Energy Storage for the Grid: A Battery of Choices. *Science* **2011**, *334*, 928-935.
- (4) Goodenough, J. B. Electrochemical Energy Storage in a Sustainable Modern

Society. *Energy Environ. Sci.* **2014**, 7, 14-18.

(5) Ellis, B. L.; Lee, K. T.; Nazar, L. F. Positive Electrode Materials for Li-Ion and Li-Batteries. *Chem. Mater.* **2010**, 22, 691-714.

(6) Choi, N. S.; Chen, Z.; Freunberger, S. A.; Ji, X.; Sun, Y. K.; Amine, K.; Yushin, G.; Nazar, L. F.; Cho, J.; Bruce, P. G. Challenges Facing Lithium Batteries and Electrical Double-Layer Capacitors. *Angew. Chem. Int. Ed.* **2012**, 51, 9994-10024.

(7) Slater, M. D.; Kim, D.; Lee, E.; Johnson, C. S. Sodium-Ion Batteries. *Adv. Funct. Mater.* **2013**, 23, 947-958.

(8) Xiao, Y.; Lee, S. H.; Sun, Y.-K. The Application of Metal Sulfides in Sodium Ion Batteries. *Adv. Energy Mater.* **2017**, 7, 299-308.

(9) Zhang, K.; Park, M.; Zhou, L. M.; Lee, G.-H.; Shin, J.; Hu, Z.; Chou, S.-L.; Chen, J.; Kang, Y.-M. Cobalt-Doped FeS₂ Nanospheres with Complete Solid Solubility as a High-Performance Anode Material for Sodium-Ion Batteries. *Angew. Chem. Int. Ed.* **2016**, 55, 12822-12826.

(10) Zhang, Y. H.; Wang, N. N.; Sun, C. H.; Lu, Z. X.; Xue, P.; Tang, B.; Bai, Z. C.; Dou, S. X. 3D Spongy CoS₂ Nanoparticles/Carbon Composite as High-Performance Anode Material for Lithium/Sodium Ion Batteries. *Chem. Eng. J.* **2018**, 332, 370-376.

(11) Zhang, Y. H.; Wang, N. N.; Xue, P.; Liu, Y. L.; Tang, B.; Bai, Z. C.; Dou, S. X. Co₉S₈@Carbon Nanospheres as High-performance Anodes for Sodium Ion Battery. *Chem. Eng. J.* **2018**, 343, 512-519.

(12) Douglas, A.; Carter, R.; Oakes, L.; Share, K.; Cohn, A. P.; Pint, C. L. Ultrafine Iron Pyrite (FeS₂) Nanocrystals Improve Sodium-Sulfur and Lithium-Sulfur

Conversion Reactions for Efficient Batteries. *ACS Nano* **2015**, 9, 11156-11165.

(13) Zhu, Y. J.; Han, X. G.; Xu, Y. H.; Liu, Y. H.; Zheng, S. Y.; Xu, K.; Hu, L. B.; Wang, C. S. Electrospun Sb/C Fibers for a Stable and Fast Sodium-Ion Battery Anode. *ACS Nano* **2013**, 7, 6378-6386.

(14) Zhu, Y. J.; Suo, L. M.; Gao, T.; Fan, X. L.; Han, F. D.; Wang, C. S. Ether-based Electrolyte Enabled Na/FeS₂ Rechargeable Batteries. *Electrochem. Commun.* **2015**, 54, 18-22.

(15) Guan, C.; Liu, J. L.; Wang, Y. D.; Mao, L.; Fan, Z. X.; Shen, Z. X.; Zhang, H.; Wang, J. Iron Oxide-Decorated Carbon for Supercapacitor Anodes with Ultrahigh Energy Density and Outstanding Cycling Stability. *ACS Nano* **2015**, 9, 5198-5207.

(16) Li, L. S.; Meng, F.; Jin, S. High-capacity Lithium-Ion Battery Conversion Cathodes Based on Iron Fluoride Nanowires and Insights into the Conversion Mechanism. *Nano Lett.* **2012**, 12, 6030-6037.

(17) Wu, R. B.; Qian, X. K.; Rui, X. H.; Liu, H.; Yadian, B.; Zhou, K.; Wei, J.; Yan, Q. Y.; Feng, X. Q.; Long, Y.; Wang, L. Y.; Huang, Y. Z. Zeolitic Imidazolate Framework 67-Derived High Symmetric Porous Co₃O₄ Hollow Dodecahedra with Highly Enhanced Lithium Storage Capability. *Small* **2014**, 10, 1932-1938.

(18) Wu, R. B.; Qian, X. K.; Zhou, K.; Wei, J.; Lou, J.; Ajayan, P. M. Porous Spinel Zn_xCo_{3-x}O₄ Hollow Polyhedra Templated for High-Rate Lithium-Ion Batteries. *ACS Nano* **2014**, 8, 6297-6303.

(19) Huang, G.; Zhang, F. F.; Du, X. C.; Wang, J. W.; Yin, D. M.; Wang, L. M. Core-Shell NiFe₂O₄@TiO₂ Nanorods: An Anode Material with Enhanced

Electrochemical Performance for Lithium-Ion Batteries. *Chem. -Eur. J.* **2014**, *20*, 11214-11219.

(20) Huang, G.; Zhang, L. L.; Zhang, F. F.; Wang, L. M. Metal-Organic Framework Derived Fe₂O₃@NiCO₂O₄ Porous Nanocages as Anode Materials for Li-Ion Batteries. *Nanoscale* **2014**, *6*, 5509-5515.

(21) Cao, X. H.; Zheng, B.; Rui, X. H.; Shi, W. H.; Yan, Q. Y.; Zhang, H. Metal Oxide-Coated Three-Dimensional Graphene Prepared by the Use of Metal-Organic Frameworks as Precursors. *Angew. Chem. Int. Ed.* **2014**, *126*, 1428-1433.

(22) Cheng, F. Y.; Tao, Z. L.; Liang, J.; Chen, J. Template-Directed Materials for Rechargeable Lithium-Ion Batteries. *Cheminform* **2012**, *39*, 667-681.

(23) Dylla, A. G.; Henkelman, G.; Stevenson, K. J. Lithium Insertion in Nanostructured TiO₂(B) Architectures. *Acc. Chem. Res.* **2013**, *46*, 1104-1112.

(24) Liu, B.; Shioyama, H.; Akita, T.; Xu, Q. Metal-Organic Framework (MOF) as Template for Porous Carbon Synthesis. *J. Am. Chem. Soc.* **2008**, *130*, 5390-5391.

(25) Liu, B.; Zhang, X. B.; Shioyama, H.; Mukaia, T.; Sakaia, T.; Xu, Q. Converting Cobalt Oxide Subunits in Cobalt Metal-Organic Framework into Agglomerated Co₃O₄ Nanoparticles as an Electrode Material for Lithium Ion Battery. *J. Power Sources* **2010**, *195*, 857-861.

(26) Pachfule, P.; Shinde, D.; Majumder, M.; Xu, Q. Fabrication of Carbon Nanorods and Graphene Nanoribbons from a Metal-Organic Framework. *Nature Chem.* **2016**, *8*, 718-724.

(27) Luo, W.; Chen, X. Q.; Xia, Y.; Chen, M.; Wang, L. J.; Wang, Q. Q.; Li, W.; Yang,

J. P. Surface and Interface Engineering of Silicon-Based Anode Materials for Lithium-Ion Batteries. *Adv. Energy Mater.* **2017**, *1701083*, 1-28.

(28) Yu, L. T.; Liu, J.; Xu, X. J.; Zhang, L. G.; Hu, R. Z.; Liu, J. W.; Ouyang, L. Z.; Yang, L. C.; Zhu, M. Ilmenite Nanotubes for High Stability and High Rate Sodium-Ion Battery Anodes. *ACS Nano* **2017**, *11*, 5120-5129.

(29) Sun J.-K.; Xu Q. Functional Materials Derived from Open Framework Templates/Precursors: Synthesis and Applications. *Energy Environ. Sci.* **2014**, *7*, 2071-2100.

(30) Wang H. L.; Zhu Q.-L.; Zou, P. Q.; Xu Q. Metal-Organic Frameworks for Energy Applications. *Chem* **2017**, *2*, 52-80.

(31) Dang, S.; Zhu, Q.-L.; Xu, Q. Nanomaterials Derived from Metal-Organic Frameworks. *Nat. Rev. Mater.* **2017**, *3*, 17075.

(32) Bai, Z. C. Zhang, X. Y.; Zhang, Y. W.; Guo, C. L.; Tang, B. Facile Synthesis of Mesoporous Mn₃O₄ Nanorods as a Promising Anode Material for High Performance Lithium-Ion Batteries. *J. Mater. Chem. A* **2014**, *2*, 16755-16760.

(33) Lu, Z. X.; Wang, N. N.; Zhang, Y. H.; Xue, P.; Guo, M. Q.; Tang, B.; Bai, Z.; Dou, S. X. Pyrite FeS₂@C Nanorods as Smart Cathode for Sodium Ion Battery with Ultra-Long Lifespan and Notable Rate Performance from Tunable Pseudocapacitance. *Electrochim. Acta* **2018**, *260*, 755-761.

(34) Xue, P.; Wang, N. N.; Wang, Y. X.; Zhang, Y. H.; Liu, Y. L.; Tang, B.; Bai, Z.; Dou, S. X. Nanoconfined SnS in 3D Interconnected Macroporous Carbon as Durable Anodes for Lithium/Sodium Ion Batteries. *Carbon* **2018**, *134*, 222-231.

- (35) Cho, J. S.; Lee, J.-K., Kang, Y. C. Graphitic Carbon-Coated FeSe₂ Hollow Nanosphere-Decorated Reduced Graphene Oxide Hybrid Nanofibers as an Efficient Anode Material for Sodium Ion Batteries. *Sci. Rep.* **2016**, 23699, 1-13.
- (36) Bai, Z. C.; Zhang, Y. W.; Zhang, Y. H.; Guo, C. L.; Tang, B. Hierarchical MoS₂@Carbon Microspheres as Advanced Anodes for Li-Ion Batteries. *Chem. - Eur. J.* **2015**, 21, 18187-18191.
- (37) Sourisseau, C.; Cavagnat, R.; Fouassier, M. The Vibrational Properties and Valence Force Fields of FeS₂, RuS₂, Pyrites and FeS₂ Marcasite. *J. Phys. Chem. Solids* **1990**, 52, 537-544.
- (38) Zhu, Y. J.; Fan, X. L.; G.; Suo, L. M.; Luo, C.; Gao, T.; Wang, C. S. Electrospun FeS₂@Carbon Fiber Electrode as a High Energy Density Cathode for Rechargeable Lithium Batteries. *ACS Nano* **2016**, 10, 1529-1538.
- (39) Xu, J.; Xue, H. T.; Yang, X.; Wei, H. X.; Li, W. Y.; Li, Z. P.; Zhang, W. J.; Lee, C.- S. Synthesis of Honeycomb-Like Mesoporous Pyrite FeS₂ Microspheres as Efficient Counter Electrode in Quantum Dots Sensitized Solar Cells. *Small* **2014**, 10, 4754-4759.
- (40) Li, J. B.; Yan, D.; Zhang, X. J.; Hou, S. J.; Li, D. S.; Lu, T.; Yao, Y. F.; Pan, L. K. In Situ Growth of Sb₂S₃ on Multiwalled Carbon Nanotubes as High-Performance Anode Materials for Sodium-Ion Batteries. *Electrochim. Acta* **2017**, 228, 436-446.
- (41) Hu, Z.; Zhu, Z. P.; Cheng, F. Y.; Zhang, K.; Wang, J. B.; Chen, C. C.; Chen, J. Pyrite FeS₂ for High-Rate and Long-Life Rechargeable Sodium Batteries. *Energy Environ. Sci.* **2015**, 8, 1309-1316.
- (42) Zhang, S. S., The Redox Mechanism of FeS₂ in Non-Aqueous Electrolytes for

Lithium and Sodium Batteries. *J. Mater. Chem. A* **2015**, *3*, 7689-7694.

(43) Shadike, Z.; Zhou, Y.-N.; Ding, F.; Sang, L.; Nam, K.-W.; Yang, X.-Q.; Fu, Z.-W.

The New Electrochemical Reaction Mechanism of Na/FeS₂ Cell at Ambient Temperature. *J. Power Sources* **2014**, *260*, 72-76.

(44) Bai, Z. C.; Zhang, Y. H.; Zhang, Y. W.; Guo, C. L.; Tang, B.; Sun, D.

MOFs-Derived Porous Mn₂O₃ as High-Performance Anode Material for Li-Ion Battery. *J. Mater. Chem. A* **2015**, *3*, 5266-5269.

(45) Brezesinski, T.; Wang, J.; Tolbert, S. H.; Dunn, B. Ordered Mesoporous

Alpha-MoO₃ with Iso-Oriented Nanocrystalline Walls for Thin-Film Pseudocapacitors. *Nat. Mater.* **2010**, *9*, 146-151.

(46) Muller, G. A.; Cook, J. B.; Kim, H.-S.; Tolbert, S. H.; Dunn, B. High

Performance Pseudocapacitor Based on 2D Layered Metal Chalcogenide Nanocrystals. *Nano Lett.* **2015**, *15*, 1911-1917.

(47) Walter, M.; Zünd, T.; Kovalenko, M. V. Pyrite (FeS₂) Nanocrystals as Inexpensive

High-Performance Lithium-Ion Cathode and Sodium-Ion Anode Materials. *Nanoscale* **2015**, *7*, 9158-9163.

(48) Wang, J.; Polleux, J.; James Lim, A.; Dunn, B. Pseudocapacitive Contributions to

Electrochemical Energy Storage in TiO₂ (Anatase) Nanoparticles. *J. Phys. Chem. C* **2007**, *111*, 14925-14931.

(49) Chen, C. J.; Wen, Y. W.; Hu, X. L.; Ji, X. L.; Yan, M. Y.; Mai, L. Q.; Hu, P.; Shan,

B.; Huang, Y. H. Na⁺ Intercalation Pseudocapacitance in Graphene-Coupled Titanium Oxide Enabling Ultra-Fast Sodium Storage and Long-Term Cycling. *Nat. Commun.*

2015, 6, 6929-6935.

(50) Chao, D. L.; Zhu, C. R.; Yang, P. H.; Xia, X. H.; Liu, J. L.; Wang, J.; Fan, X. F.; Savilov, S. V.; Lin, J. Y.; Fan, H. J.; Shen, Z. X., Array of Nanosheets Render Ultrafast and High-Capacity Na-Ion Storage by Tunable Pseudocapacitance. *Nat. Commun.* **2016**, 7, 12122-12130.

(51) Augustyn, V.; Come, J.; Lowe, M. A.; Kim, J. W.; Taberna, P-L.; Tolbert, S. H.; Abruna, H. D.; Simon, P.; Dunn, B., High-Rate Electrochemical Energy Storage Through Li^+ Intercalation Pseudocapacitance. *Nat. Mater.* **2013**, 12, 518-522.

■ Table of Contents

